Structure of the orthorhombic Al₁₃Co₄(100) surface using LEED, STM, and *ab initio* studies

Heekeun Shin,[1] K. Pussi,[2] É. Gaudry,[3] J. Ledieu,[3] V. Fournée,[3] S. Alarcón Villaseca,[3] J.-M. Dubois,[3] Yu. Grin,[4] P. Gille,[5] W. Moritz,[5] and R. D. Diehl[1,*]

[1]*Department of Physics, Penn State University, University Park, PA 16802, USA*
[2]*Department of Mathematics and Physics, Lappeenranta University of Technology, P.O. Box 20 FIN-53851 Lappeenranta, Finland*
[3]*Department CP2S, Institut Jean Lamour, École des Mines, Parc de Saurupt, 54042 Nancy Cedex, France*
[4]*Max-Planck-Institut für Chemische Physik fester Stoffe, Nöthinitzer Str. 40, 01187 Dresden, Germany*
[5]*Department of Earth and Environmental Sciences, Crystallography Section, LMU, Theresienstr. 41, D-80333 München, Germany*

In a combined scanning tunneling microscopy (STM), low-energy electron diffraction (LEED), and density functional theory (DFT) study of the surface of Al₁₃Co₄(100), all techniques have found that after annealing to 1165 K, the surface structure is consistent with a dense Al-rich plane with surface Co atom depletion. Various structure models were considered, and in the LEED study, the best agreement was found with a model that consists of Al-rich terminating planes with no Co atoms, and otherwise a structure similar to the bulk puckered layers. This structure was also found to be stable in the DFT study. The best-fit structural parameters are presented for the two domains of this structure, which contain bipentagons that can be related to the pentagonal bipyramidal structures in the bulk, plus additional glue atoms between them. These domains are not strictly related to each other by symmetry, as they have different surface relaxations. The STM study found significant differences in the surfaces of samples grown by different methods and is able to explain a different interpretation made in an earlier study.

I. INTRODUCTION

The aperiodic surfaces of quasicrystals have different physical properties from their periodic counterparts. For instance, they have lower coefficients of friction and lower adhesion energies against polar liquids.[1] Because their unit cells are infinite, they are often modeled using structures that have the same local arrangements but which, unlike quasicrystals, are periodic over a longer range, so-called quasicrystal approximants.[2–4] Due to the complexity of the structures, it can be difficult to ascertain in a quantitative way the degree to which the finite unit cell structures replicate the aperiodic crystals, i.e. are discrepancies due to the imperfect modeling methods or due to the model structure itself? It is also the case that the powders used for quasicrystalline coatings likely have a significant fraction of particles with periodic structures that are near to the quasicrystalline phase in the alloy phase diagram. For these reasons, it is desirable to study some examples of the quasicrystal approximants. In the past few years, several examples[5] of periodic complex metallic alloys have been grown in sizes large enough to investigate using experimental surface science methods.

Orthorhombic Al₁₃Co₄ is a complex metallic alloy that is an approximant of the decagonal Al-Co-Ni quasicrystal, and its (100) surface is an approximant of the 10-fold quasicrystal surface.[6,7] Al₁₃Co₄ has a unit cell containing just 102 atoms, and it contains the same basic pentagonal bipyramidal structure elements as the decagonal quasicrystal.[7] The crystal structure of o-Al₁₃Co₄ was first investigated from single crystal diffraction data and described in the space group *Pmn*21.[8] From these data, it was recognizable that there is some disorder present in the layers perpendicular to [100]. The re-investigation of the crystal structure from high-resolution single-crystal diffraction data[9] was able to

resolve the disorder and to derive three ordered models with 102 atoms per unit cell, representing distortion variants of the pseudopentagonal columnar structural units characteristic for this group of complex metallic phases. The structure can be described as the stacking along the [100] direction of two types of layers, flat (*F*) having 17 Al and 8 Co atoms, and puckered (*P*), having 22 Al and 4 Co atoms per unit cell. There are two types of each plane, producing a stacking sequence $F_1 P_1 F_2 P_2$ and a separation between planes of about 2 Å. This structure has $Pmn2_1$ symmetry, and the mirror plane is coincident with an *F* plane, i.e. parallel to the (100) surface.

The structures of the *F* and *P* layers are different, as shown in Fig. 1. The *F* layers can be described by a pentagon-and-rhombus tiling by connecting the Co atoms. Here, F_1 is related to F_2 by a translation of half a unit cell in the *c* direction and then a reflection through an *ac* plane. This is a glide operation with glide vector $(a + c)/2$. Normally, a glide plane along the *c* direction would be expected to cause an extinction of the (0, *k*) beams with *k* odd if the scattering plane lies parallel to the glide plane. However, extinction is not expected in this case if the surface contains both F_1 and F_2 terminations because the scattering from different terraces is incoherently averaged. A single *F* terrace termination has no symmetry; however when the two *F* planes are averaged, there is an overall mirror symmetry along the *c* direction.

The *P* layers are described by a different tiling composed of elongated hexagons as shown in Fig. 1(d). The direction of the pucker in P_1 is related to that in P_2 by a mirror reflection with respect to the intervening *F* layer. An array of pentagonal bipyramid clusters that are the basic building blocks of this structure, and also the related decagonal quasicrystal, extend perpendicularly through these layers. The *P* layers do not exhibit the glide symmetry of the *F* layers due to its nonplanar
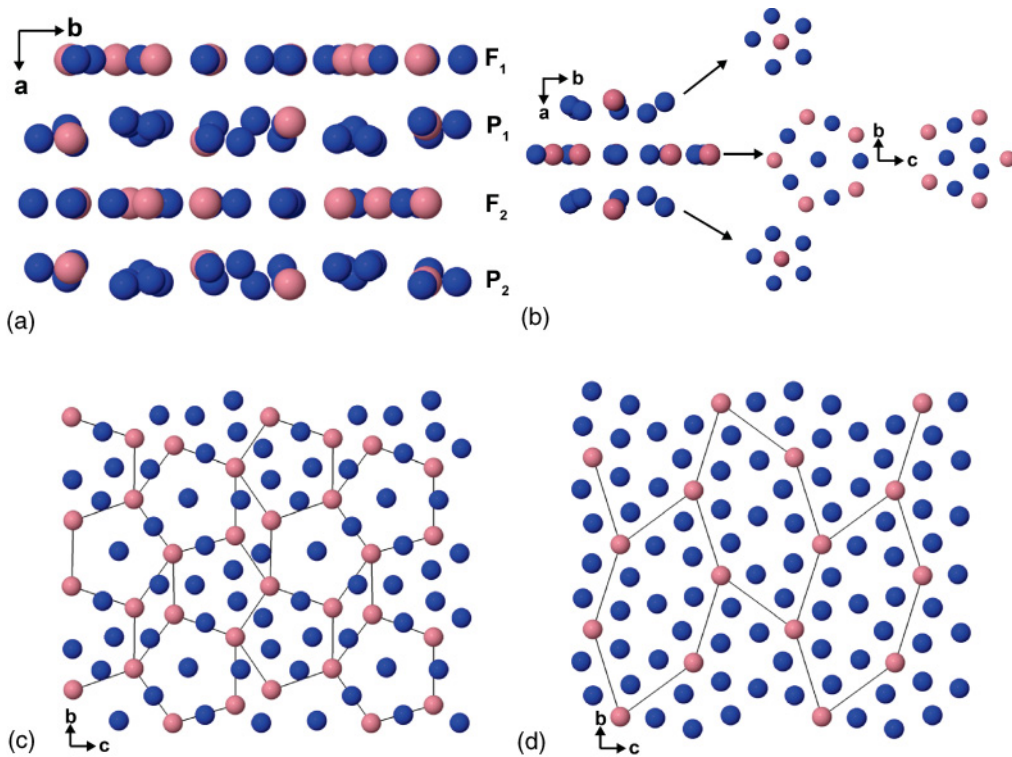
FIG. 1. (Color online) The bulk structure of $Al_{13}Co_4$. The dark (blue) spheres are aluminum and the light (pink) spheres are cobalt. (a) Side view of the unit cell, composed of four layers of atoms. (b) Side view (left) of the pyramid structure, and a top view (right) of each layer. The registry of the center F layer is different for F_1 and F_2; both are shown. (c) Top view of F layer. (d) Top view of P layer.

structure, but averaging the two P layers produces mirror symmetry along the c direction, as for the F layers.

Analysis of the chemical bonding in o-$Al_{13}Co_4$ using an electron density/electron localizability approach[9,10] revealed numerous covalent Co-Al and Al-Al bonds within the P and F layers (more in F than in P) as well as between P and F layers. A special feature obtained from the analysis was the formation of the linear Co-Al-Co groups aligned along [100]. Combination of the presence of the F planes and the Co-Al-Co groups opens the possibility of special atomic arrangements in the termination planes.

A recent scanning tunneling microscopy (STM) study[11] found that the surface termination of this crystal depends strongly on the preparation procedures. The procedure used in this case involved the fairly standard method of cycles of Ar^+ ion bombardment followed by extensive annealing. For annealing times of at least 2 h at temperatures of 1115 K, atomically flat terraces having similar structures and separated by 4.2 Å steps were observed. The average terrace size grew with additional annealing, revealing the presence of two types of terminations, separated by steps of 2.2 Å. The two terminations were denoted $T1$ and $T2$, and annealing to 1165 K resulted in the preferential removal of $T2$, leaving a surface almost entirely composed of $T1$. The conclusion of a detailed study of $T1$ was that this termination consists of an incomplete P layer, described in more detail later. A related *ab initio* study carried out to simulate the STM images showed consistency between the model deduced from the STM and the simulated STM images.[11] Following that study, additional *ab initio* studies were performed, as described below.

While STM excels at detecting the qualitative structure and morphology of the surface, it is much more difficult to measure parameters such as the layer registry and surface relaxation. For these, a scattering technique that is sensitive to several layers is advantageous. Low-energy electron diffraction (LEED) is the primary technique for quantitative surface structure analysis, but has only recently been applied to complex surfaces because its computational requirements increase rapidly with the size of the unit cell.[12,13] Increased computing capacity and speed brings new power to LEED, but also new challenges, including the acquisition of enough experimental data for the increased parameter space of complex structures and the ability to generate the appropriate model structures. Without additional information, generating and testing all possible model structures is impossibly time consuming, and this is where the input from other techniques, in this case STM and *ab initio* calculations, is invaluable. To our knowledge, the study presented here has the largest unit cell ever analyzed with LEED and the largest experimental data set, about four times larger than the next-largest one.[14]

II. STRUCTURE MODELS

As described above, the bulk structure of $Al_{13}Co_4$ consists of two types of planes in the (100) direction, F and P. The STM study concluded that the $T1$ termination to which the surface converts upon annealing is a P layer. It also concluded that not all atoms in the P layer are present in the surface layer. Therefore, we have constructed two types of models for P-layer terminations: the complete (or nearly complete) P
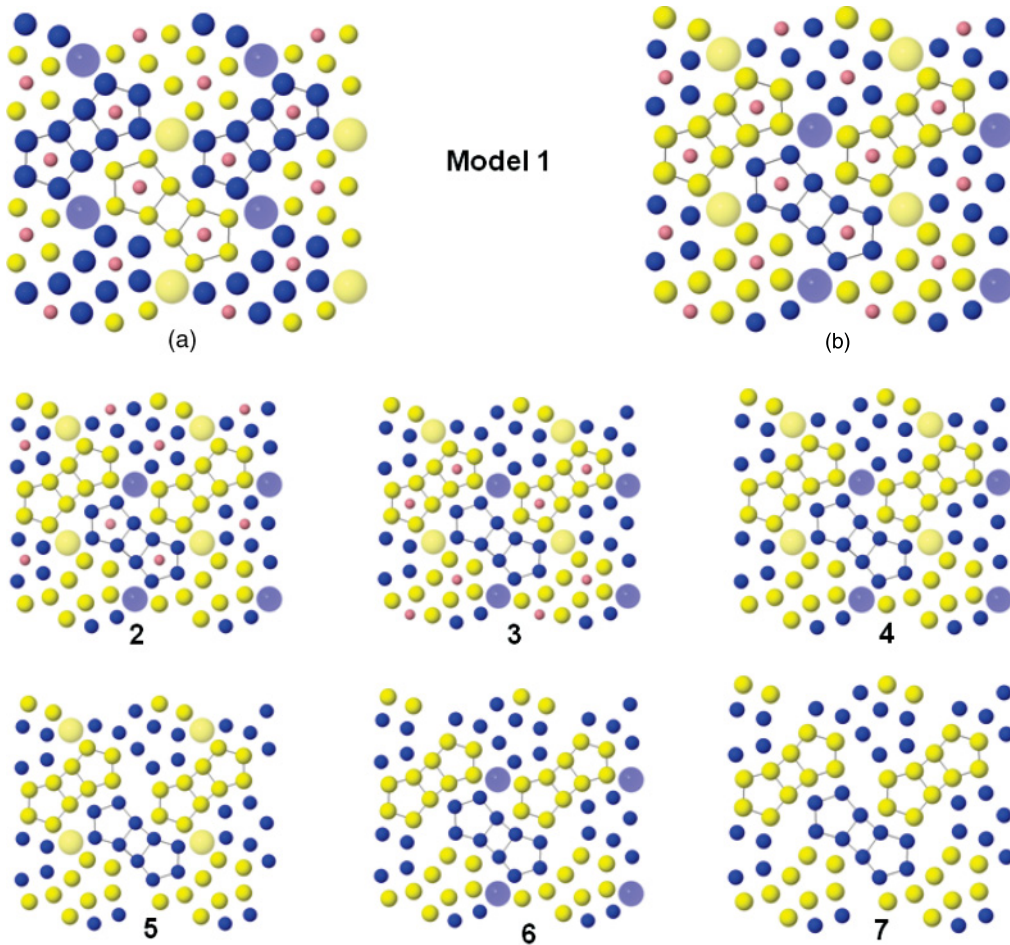
FIG. 2. (Color online) The model structures of complete P-layer termination. (a) and (b) show the two different P layers, P_1 and P_2, indicating the bipentagon features. The models are numbered as described in the text. Small (pink) circles indicate the Co atoms, present only in models 1–3. The larger circles correspond to Al glue atoms. The remaining blue (yellow) circles correspond to Al atoms above (below) the center of mass of the P layer.

layer, and the incomplete P layer, in which about half of the surface atoms are absent. We also constructed models based on an F-layer termination, for comparison.

Figure 2 shows several variations of the P-layer model. Only the P_2 models are shown here, but corresponding P_1 models were also included in the LEED analysis since the surface studied is expected to include both terminations. In each complete P layer, there are four Co atoms per surface unit cell. In the bulk planes, two of them reside above the center of mass of the P layer, and two reside below. We have generated four models from this complete (or almost complete) P-layer model, which include (1) all four Co atoms, (2) only the bottom Co atoms, (3) only the top Co atoms, and (4) no Co atoms. In the bulk structure, there are two Al atoms per unit cell that reside between the bipentagons of the puckered layer. The presence or absence of these glue atoms gives three additional models to consider, all of which start with model (4) and are: (5) minus one Al glue atom, (6) minus the other Al glue atom, and (7) minus both Al glue atoms. Models with Co atoms where glue atoms are removed were not considered because the initial results using LEED (see below) indicated a clear preference for the absence of Co atoms.

Figure 3 shows several variations of the P termination where only one set of bipentagons is present, described here as an incomplete P-layer model. The motivation for these models came from the STM images, where just one set of the bipentagons was clearly visible. The variations of this model that were tested include the incomplete model with the bipentagons (8) with the top Co atoms and (9) without Co atoms, and the incomplete model with the bipentagons (10) containing the bottom Co atoms and (11) without the Co atoms. None of these structures include the glue atoms. For completeness, we also tested models based on the F termination structure. Figure 4 shows the models that comprise (12) the complete F-layer model and (13) the F-layer without Co atoms.

III. *AB INITIO* CALCULATIONS AND RESULTS

A. Calculation methods

Our *ab initio* calculations are based on the density functional theory (DFT) framework. They have been performed with the Vienna *ab initio* simulation package (VASP).[15,16]
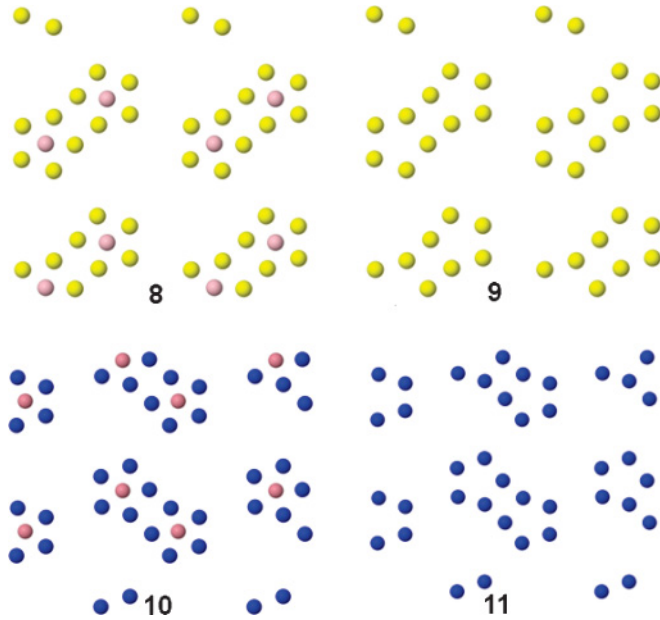
FIG. 3. (Color online) The model structures of incomplete P_2-layer termination. The color code is the same as that shown in Fig. 2.

The projector-augmented wave (PAW) method[17,18] is used to describe the interaction between the valence electrons and the ionic core. Electronic exchange and correlation is described by the generalized gradient approximation Perdew-Burke-Ernzerhof (PBE).[19,20]

Although the present calculations are called *ab initio*, there are convergence parameters linked to the numerical implementation of the density functional theory framework. Two of them are the plane-wave cutoff energy E_{cut} and the
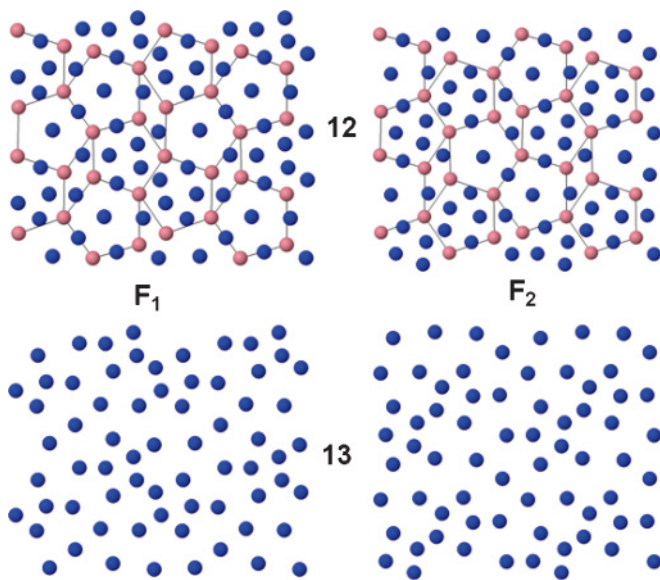

FIG. 4. (Color online) The model structures of the F-layer terminations. The color code is the same as that shown in Fig. 1.

density of k points sampling the Brillouin zone. We have, by means of a series of test calculations on bulk $Al_{13}Co_4$ (102 atoms/cell), determined the values for E_{cut} (400 eV) and the size of the Monkhorst–Pack k-points mesh ($6 \times 4 \times 4$) to achieve a target precision for the total energy smaller than 1.5 meV/atom. For the calculations using slabs, we have used a ($1 \times 4 \times 4$) k-grid mesh.

The optimization of the atomic coordinates (and unit cell dimensions for bulk material) is performed via the calculation of the Hellmann–Feynman forces acting on atoms and their minimization via a conjugate gradient algorithm. Simulations of the (100) surfaces of $Al_{13}Co_4$ are achieved by building asymmetric slabs separated by a 15 Å thick vacuum region. All slabs have the same bottom-ending layer; they differ only by the topmost atomic layer. Due to the large size of the $Al_{13}Co_4$ crystal cell, and since we are interested here in qualitative results concerning STM image simulations and in relative surface determination, we have decided to do all *ab initio* calculations with six-layer-thick slabs. These slabs are built as follows: the two atomic layers at the bottom are kept fixed, while the four remaining layers are relaxed. We check that the six-layer slab thickness is enough for relative surface energy calculations and qualitative STM simulations: the STM images simulated for models 1 and 3 using the previous six-layer-thick slabs or eight-layer-thick slabs (four fixed and four mobile atomic layers) are the same. The surface energy difference $\gamma_1 - \gamma_3$ has been evaluated to be the same within 1 meV Å^{-2}. In the following, surfaces described as stable are those that minimize the relative surface energy to within 5 meV. STM images have been simulated from electronic structure calculations by considering surfaces of constant local density of states integrated over an energy window from E_F to $E_F + V_{bias}$, where V_{bias} is the voltage applied between the sample and the tip. The bias V_{bias} and the tip-sample distance d have been chosen to match the experimental setting ($V_{bias} = -1.3$ V).

B. Results

Optimization of the bulk $Al_{13}Co_4$ leads to the following cell parameters: $a = 8.20$ Å, $b = 12.40$ Å, and $c = 14.42$ Å. The latter are in good agreement with the experimental data[8] ($a = 8.158$ Å, $b = 12.342$ Å, and $c = 14.452$ Å), as well as with previous calculations.[21] Total energy calculations yield (i) the formation energy of the alloy $\Delta H_f = -0.39$ eV/atom, where $\Delta H_f = \mu_{Al_{13}Co_4}^{bulk} - 13\mu_{Al}^{bulk} - 4\mu_{Co}^{bulk}$, which is also in good agreement with the value reported in Refs. 21 and 22 (-0.41 eV/atom). In the following, the considered slabs are built from the bulk crystal structure and the calculations are based on the P_2-layer models described above.

1. Energetics

The surface energies corresponding to structural models that differ by the topmost atomic layer cannot be compared directly by calculating the total energies of the corresponding slabs. In order to analyze the relative surface stability of surfaces with different stoichiometries, we follow the methodology proposed in Refs. 23–25.

The relative surface energy $\gamma_{surf}^\alpha - \gamma_{surf}^1$ of the termination of model α compared to the one of model 1 (α and 1 are the labels of the considered structural models, see Figs. 2, 3, and 4)

is evaluated from the total energy of the corresponding slabs by

$$\gamma_{\text{surf}}^{\alpha} - \gamma_{\text{surf}}^{1} = \frac{1}{A}\Big[E_{\text{slab}}^{\alpha} - E_{\text{slab}}^{1} - \big(N_{\text{Al}}^{\alpha} - N_{\text{Al}}^{1}\big)\mu_{\text{Al}}$$
$$- \big(N_{\text{Co}}^{\alpha} - N_{\text{Co}}^{1}\big)\mu_{\text{Co}}\Big],$$

where E_{slab}^{α} (E_{slab}^{1}) is the total energy of the slab labeled α (1), A is the surface area, μ_i are the chemical potentials for each species i, N_i^{α} (N_j^{1}) is the number of i-type atoms in the slab α (1). It is possible to rewrite the previous equation with just one chemical potential, for example μ_{Al}, using the equation expressing the thermal equilibrium between the surface and the bulk: $\mu_{\text{Al}_{13}\text{Co}_4} = 13\mu_{\text{Al}} + 4\mu_{\text{Co}}$. The relative surface energy $\gamma_{\text{surf}}^{\alpha} - \gamma_{\text{surf}}^{1}$, can then be written as follows:

$$\gamma_{\text{surf}}^{\alpha} - \gamma_{\text{surf}}^{1} = \frac{1}{A}\Big[E_{\text{slab}}^{\alpha} - E_{\text{slab}}^{1} - (M^{\alpha} - M^{1})\mu_{\text{Al}}$$
$$- \frac{1}{4}\big(N_{\text{Co}}^{\alpha} - N_{\text{Co}}^{1}\big)\mu_{\text{Al}_{13}\text{Co}_4}\Big],$$

where $M^j = N_{\text{Al}}^j - \frac{13}{4}N_{\text{Co}}^j$ (j is for label 1 or α). Since Al and Co elements form an alloy rather than segregate ($\Delta H_f < 0$), the chemical potential μ_i of the species i in the alloy has to be smaller than the corresponding bulk chemical potential μ_i^{bulk}. These conditions give the variation range for μ_{Al}: $\frac{\Delta H_f}{13} < \mu_{\text{Al}} - \mu_{\text{Al}}^{\text{bulk}} < 0$.

Figure 5 shows the relative surface energies $\gamma_{\text{surf}}^{\alpha} - \gamma_{\text{surf}}^{1}$ as a function of μ_{Al}. The surfaces 10 and 11 are not stable compared to the other structural models. This result can be understood by the low atomic density of models 10 and 11 (the surface unit cell contains 12 and 10 atoms, respectively) compared to the almost-complete P-layer models (models 1–7). Models 8 and 9 also present low surface atomic densities, but they are more stable. Their increased stability relative to models 10 and 11 is explained by the bonding interactions between the atoms in the F layers and the Co-Al-Co groups aligned along [100].[9,26,27] The surface models 10 and 11 result from a cut
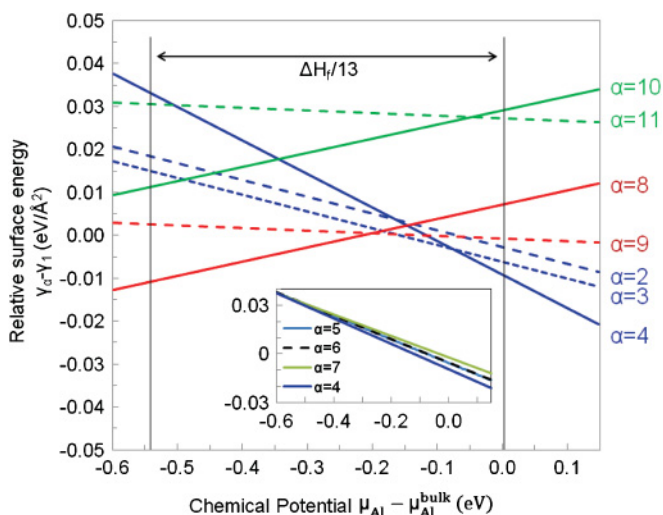

FIG. 5. (Color online) Relative surface energy (relative to model 1) vs the chemical potential μ_{Al} for the 11 different surface models shown in Figs. 2–4. The inset shows magnified results for the surface model 4 and its derivatives (models 5, 6, and 7).

through this Co-Al-Co molecular group, while models 8 and 9 preserve the Co-Al-Co molecular structure at the surface.

When comparing the almost complete P-layer models, it appears that for $\mu_{\text{Al}} = \mu_{\text{Al}}^{\text{bulk}}$, the surface energy is lower for model 4 compared to models 3, 2, and 1. This correlates with the higher percentage of Co surface atoms in models 3, 2, and 1 ($\geqslant 2$ atoms per surface unit cell) compared to model 4 (no Co surface atoms). In addition, the Co atoms in model 3 are slightly below the mean position of the surface plane, while for model 2, they are slightly above. Therefore, the presence of surface Co atoms seems to contribute to surface destabilization. This can be associated with the higher elementary surface energy of Co [2.522 J m^{-2} (Ref. 28), 2.550 J m^{-2} (Ref. 29)] compared to Al [1.143 J m^{-2} (Ref. 28), 1.160 J m^{-2} Ref. 29)]. Therefore, models 4, 5, 6, and 7, which have no Co atoms and only differ by the presence or absence of glue atoms, appear to have the most stable structures. After optimization, there was little change of the top interlayer spacing for these structures, which was found to be about 2.04 Å relative to the bulk value of 2.05 Å.

2. STM images

Two sets of experimental images were acquired on two different samples of the same phase. Sample 1 was grown by the Bridgman method in Jülich. The initial melt composition was Al$_{84.5}$Co$_{15.5}$. Sample 2 was grown by the Czochralski method in Nancy. The initial melt composition was Al$_{85}$Co$_{15}$. The composition range of the o-Al$_{13}$Co$_4$ crystal is very narrow; with a Co content comprised between 23.9 and 24.4 atomic % according to Ref. 5. Therefore, the compositions of both crystals can be considered as equivalent. The crystals were oriented using Laue x-ray diffraction, cut perpendicular to the [100] direction, and then mechanically polished using diamond paste with decreasing grain size down to 0.25 μm and using Syton for the final polishing. A clean surface was obtained by repeated cycles of 1–2 keV Ar$^+$ bombardment and annealing in the range between 1070 and 1170 K in ultra-high vacuum. The annealing temperature of the crystals was measured using an infrared pyrometer with the emissivity set at 0.35.

Typical high-resolution STM images obtained on both samples are shown in Fig. 6 and reveal a different contrast. The image in Fig. 6(a) corresponds to sample 1. It was interpreted in our previous report as consisting of an incomplete puckered layer where just one set of bipentagons containing the bottom Co atoms remains at the surface.[9] This corresponds to model 10 (see Fig. 3). In addition, glue atoms connecting the bipentagonal features are also observed with a random occupancy, but many of them are missing. An alternative possibility could be that this surface corresponds to model 10 with the other set of Al bipentagons being present but not visible in STM images because this other set of bipentagons lies slightly below the mean position of the plane. However, the root-mean-square (RMS) roughness is 0.42 ± 0.05 Å and peak-to-peak roughness is 2.1 ± 0.2 Å for sample 1. This could be interpreted as evidence that the second set of bipentagons has desorbed. However, STM probes the variation of the electronic density of states and not directly the surface topography.

The STM image in Fig. 6(b) is characteristic of sample 2 and shows a different contrast compared to sample 1. Individual
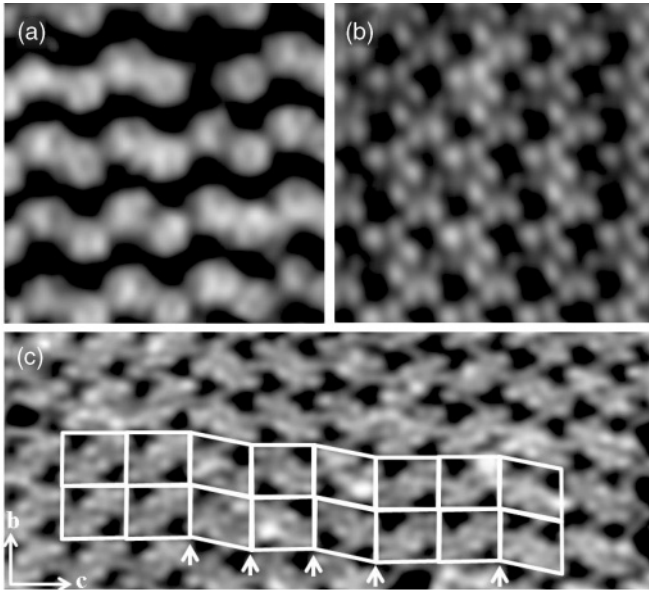
FIG. 6. STM images (6×6 nm^2) of the (100) surface terminations of sample 1 [(a), $V = -1.3$ V] and of sample 2 [(b), $V = -0.6$ V]. (c) STM image (15 nm $\times$ 6 nm, $V = -0.6$ V) obtained on sample 2 showing twin planar defects in the (100) surface. A tiling is superimposed, with rectangular (orthorhombic) and oblique (monoclinic) cells. Arrows indicate domain boundaries.

atoms forming the bipentagonal features are now resolved. The four central atoms of each bipentagonal motif are imaged as two elongated bright features. Height profiles across the bipentagonal features reveal that their centers are frequently populated with an atom lying below the five Al atoms (a Co atom according to the model). The two types of glue atoms connecting the bipentagons are also observed. As a result, the surface plane is more compact than that observed on sample 1.

The roughness measured on individual terraces is also lower on sample 2 compared to sample 1. The RMS roughness is 0.11 ± 0.02 Å and peak-to-peak roughness is 0.5 ± 0.1 Å. Again, it is likely that the second set of bipentagons is present but appears with a dark contrast in the images because they lie 0.25 ± 0.1 Å below the mean position of the plane. Simulated STM images will confirm this hypothesis in the following section.

Another difference between the two samples is the presence of special defects observed on some parts of the surface of sample 2, which we did not observe on sample 1. It is manifested by an inversion of the bipentagonal motifs with respect to the (001) plane and shifted along [010] by $b/(1 + \tau) = 0.38b = 0.47$ nm.[30] This is clearly seen in Fig. 6(c) for both sets of bipentagons with either bright or dark contrast. A tiling has been overlaid on the image in Fig. 6(c) where the nodes are located at the centers of bipentagonal features with dark contrast. These defects result in the transformation from a rectangular orthorhombic unit cell to an oblique cell similar to that expected for the monoclinic m-Al$_{13}$Co$_4$ approximant. Similar observations for bulk materials using high-resolution electron microscopy have been reported earlier and in fact occur quite frequently in Al$_{13}$TM$_4$ phases (TM = transition metal).[30–32] All of these phases contain similar pentagonal columns and are related to each other by slightly different arrangements of these columns.

The calculated STM images for models 1 to 11 are shown in Fig. 7. Comparing first with the experimental STM contrast for sample 1 [Fig. 6(a)], it is quite clear that the almost complete *P*-layer models 1, 2, and 3 do not provide a good match, since no isolated bipentagonal features appear in the simulation. A better agreement is achieved with the simulated STM images corresponding to model 4 and its derivatives, models 5, 6, and 7. The bright bipentagonal motifs are associated with aluminum bipentagons slightly above the mean position of the plane ($+0.28$ Å). The atoms of the other
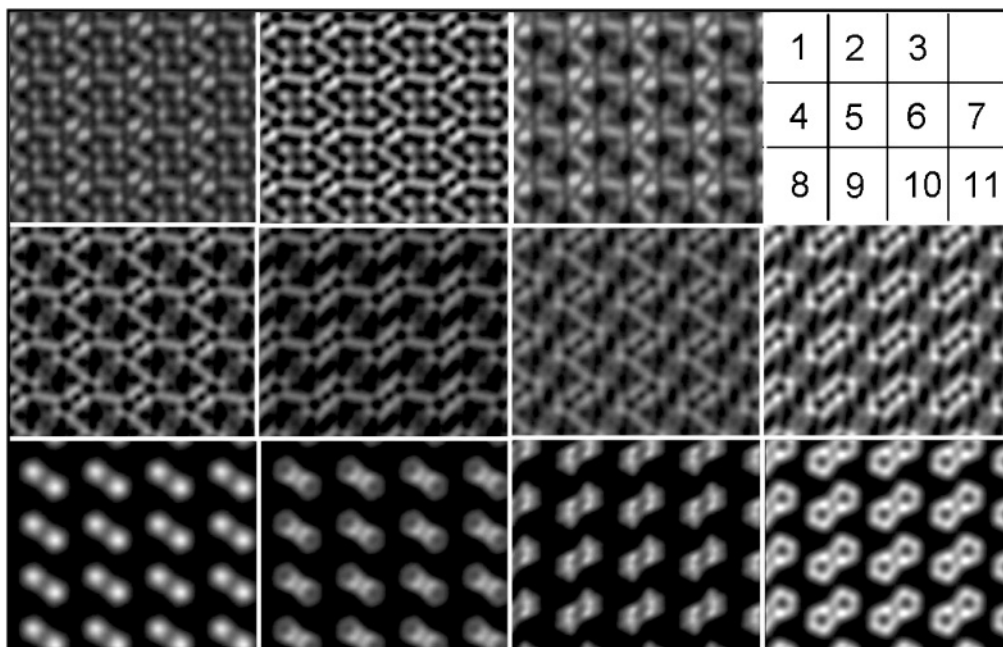

FIG. 7. Simulated STM images at $V_{\rm bias} = -1.3$ V for the models 1 to 11 considered. Each image spans an area of (4×4) unit cells.

bipentagons lie slightly below (-0.25 Å) the mean position of the plane, hence they appear with a darker contrast in the STM image.

The model 8 with only one set of bipentagons remaining with Co atoms on top leads to a simulated STM image characterized by two very bright points due to the presence the protruding Co atoms. This model is clearly not compatible with the STM image since the centers of the pentagons appear as depressions in Fig. 6(a). Low-density models 9 and 11, where the surface plane consists of only one set of bipentagons and no Co atoms, lead to the best agreement with the experimental image obtained for sample 1. The model 10 with the Co atoms below the bipentagons is also compatible with the experiment. However, the models 10 and 11 appear highly unrealistic based on relative surface energy DFT calculations presented above. In addition, we have recently reported the formation of rows extending along [010] upon Pb deposition on the surface of sample 1. These rows can only be reproduced by DFT calculations for dense substrate models where both sets of Al bipentagons are present. Therefore, models 4 to 7 are the most likely to account for the surface structure observed on sample 1.

If we now compare the simulated images with the STM contrast obtained on sample 2 [Fig. 6(b)], it is clear that low-density models 9 to 11 can be disregarded. The complete *P* layer (model 1) and model 2 with top Co atoms do not fit either. There is an excellent agreement with model 3 (complete *P* layer without top Co atoms) as well as with model 4 but to a lesser extent (complete *P* layer without any Co atoms). Models 5 to 7 can be disregarded as well, as all glue atoms are present in the experimental image. The presence of all glue atoms on sample 2 results in a smaller roughness and improved resolution by STM, providing evidence for the presence of bottom Co atoms (model 3). However, we cannot affirm from STM images that these Co sites are fully occupied over the entire surface area. If this was the case, the surface of sample 2 will consist of a mixture of models 3 and 4.

To summarize, the comparison between simulated and experimental images points toward a *P*-layer surface termination where both sets of Al bipentagons are present and top Co atoms have desorbed. Depending on samples, the density of Al glue

atoms varies, resulting in a less stable surface termination according to DFT calculations.

IV. LEED EXPERIMENT, CALCULATIONS AND RESULTS

A. Experiment

The Al$_{13}$Co$_4$ sample used in this study was grown from Al-rich solutions using the Czochralski method in Munich,[5] which is the same method as for sample 2 in the STM study discussed earlier. The crystal was oriented using Laue x-ray diffraction, cut perpendicular to the [100] direction, and then mechanically polished using diamond paste with decreasing grain size down to 0.25 μm and using Syton for the final polishing. In ultra-high vacuum, a procedure similar to that followed in the STM study was followed, with cycles of 0.5 keV Ar+ bombardment and annealing as high as 1170 K. The annealing temperature of the crystal was measured using an infrared pyrometer with the emissivity set at 0.35. The LEED patterns after this procedure were similar to those observed under similar conditions in the STM experiments, shown in Fig. 8. Although the unit cell of the structure has no symmetry, the LEED pattern has two apparent mirror planes along the perpendicular principle axes of the diffraction pattern. From the symmetry of the bulk structure described earlier, and assuming equal amounts of the two *P* (or two *F*) terminations, we would expect to have a mirror plane along the direction corresponding to the vertical axis in the LEED patterns in Fig. 1. However, inspection of the LEED patterns and of the intensity curves indicates also mirror symmetry along the horizontal axis. While a mirror symmetry along this axis is not a true symmetry when considering two *P* or two *F* terminations of the structure, it is apparently close enough to make the LEED intensities indistinguishable. We note also that the relative intensities of the diffraction spots at 50 eV (not shown) observed for this sample are the same as those observed in the STM study for sample 2, but not sample 1.

The LEED measurements were carried out for a sample temperature of 80 K using a VG Scientific 2-grid LEED optics. The patterns were acquired using a frame grabber card interfaced to a PC, and the intensities were extracted using the in-lab HotLEED software. The extraction of the intensities
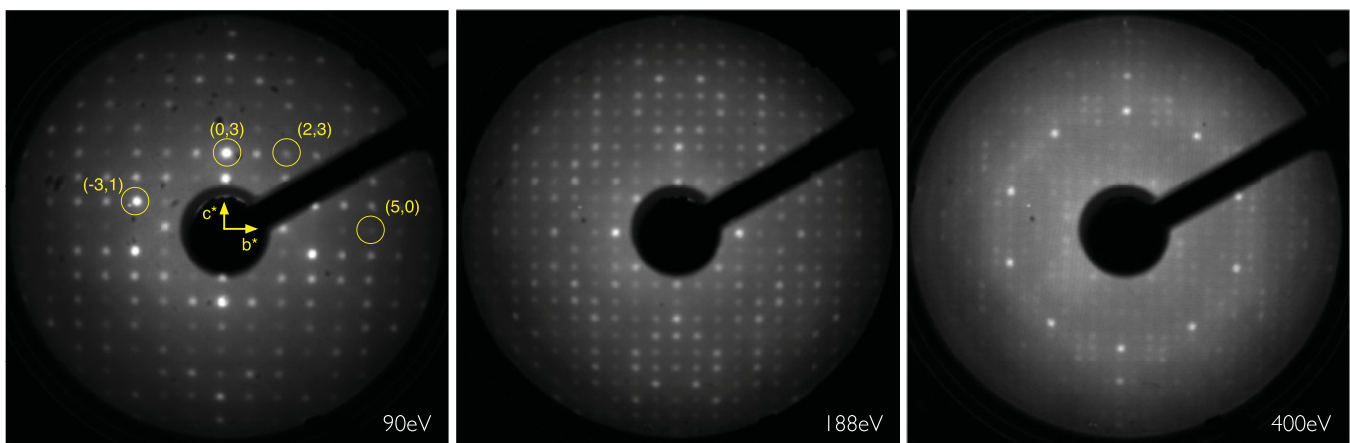

FIG. 8. (Color online) LEED patterns from Al$_{13}$Co$_4$ at a sample temperature of 80 K, for beam energies 90, 188, and 400 eV. The beam indices are indicated for selected beams.

involved integration of the spot intensities and subtracting a background equal to the perimeter intensity of the spot. The intensities from symmetry-equivalent beams were averaged assuming two perpendicular mirror planes, and the final dataset consists of 69 symmetry-nonequivalent beams, with a total energy range of 19 640 eV. The acquisition of such a large data set was possible due to the high density of diffraction beams (from the large unit cell), the relatively low symmetry of the structure, and by acquiring the data at low temperature to minimize thermal scattering.

B. Calculations

The procedure for structure determinations using LEED involves the assumption of a model structure, computation of the intensity spectra for that model structure, and comparison of the calculated spectra to the experimental spectra using the Pendry reliability factor (R factor).[33] These calculations were performed using the SATLEED suite of programs.[34] This program includes an automated search algorithm, which searches for the best fit (minimum R factor) between the experimental and calculated spectra. The phase shifts for the surface layer and for the deeper layers were calculated from the Van Hove package[34] using up to 12 phase shifts determined that nine phase shifts were required for the LEED calculations. The imaginary part of the potential was fixed at -5 eV. Because of the mirror symmetry exhibited in the experimental intensity curves, the structure optimization was carried out assuming two perpendicular mirror planes, which averages the intensities for the four symmetry-equivalent structures. These calculations were carried out separately for each termination, P_1, P_2, F_1, and F_2. As described before, each termination by itself has no symmetry, only the average of the two P or two F terminations has the (c axis) mirror symmetry. Therefore, the two P or F terminations should have their intensities mixed before optimizing the structure. However, because there was no facility in the SATLEED program for

calculating and optimizing two terminations simultaneously, we performed the optimization (assuming two mirror planes) for each termination separately and then averaged them. Although this is not the most rigorous procedure, we believe that our results justify it, as explained in Sec. V.

In the structural analysis, up to four layers of atoms (=98 atoms) were relaxed. The complete three-dimensional optimization of the positions of the 98 atoms in the unit cell, plus the real part of the inner potential, produces 294 adjustable parameters during the search. Since the total energy range is 19 640 eV, this gives 67 eV per adjustable parameter. Both the rule of thumb requiring at least 50 eV per parameter and the number of features (peaks and dips) in the diffraction spectra being at least as great as the number of parameters are satisfied in this analysis. However, it was necessary to be very cautious of local R-factor minima during the optimization procedure. The most reliable results were obtained by optimizing first the top layer in the z direction (i.e. perpendicular to the surface plane), then the top two layers, etc. until all four layers were optimized in the z direction. Then, the 3D optimization was performed for all four layers. The full calculation, during the final optimization, has a calculation time of 460 h for one run on a Murska super cluster. In order to make the computational time more manageable, the calculation was split into 46 parts, each taking about 10 h on a separate node of the cluster.

C. Results

Table I includes the best-fit R factors for all of the tested models. It is quite clear that the F termination, with a best R factor of 0.45, is not a good fit, which was expected from the STM result. The best R factor from the incomplete P-layer models was 0.38, which is also not a very good result. The R factors for the complete (or almost complete) P-layer models ranged up to 0.41, but removing the Co atoms from these models improved the fit significantly, and the best result was 0.26 for the complete P layer with no Co and both glue

TABLE I. Structure models, DFT results, and LEED R factors. The STM simulations for sample type 2 find that model 3 is the best fit, and model 4 is an acceptable fit. The LEED study finds that model 4 is the best fit.

Model	DFT stability	DFT-STM fit	LEED R factor
Complete puckered top with:			
1. All Co atoms	Yes	No	0.35
2. Only high Co atoms	Yes	No	0.41
3. Only low Co atoms	Yes	Yes	0.31
4. No Co atoms	Yes	Yes	0.26
5. No Co and without Al-1 glue atom	Yes	No	0.30
6. No Co and without Al-2 glue atom	Yes	No	0.29
7. No Co and without both glue atoms	Yes	No	0.32
Incomplete-1 puckered top with:			
8. High Co atoms	Yes	No	0.40
9. No high Co atoms	Yes	No	0.38
Incomplete-2 puckered top with:			
10. Low Co atoms	No	No	0.48
11. No low Co atoms	No	No	0.42
Complete flat top with:			
12. Co atoms present	N/A	No (Ref. 11)	0.45
13. No Co atoms	N/A	N/A	0.57

P₁ parameters	(Å)
dz(P1-F2)	2.06 ± 0.05
dz(F2-P2)	2.02 ± 0.06
dz(P2-F1)	2.05 ± 0.09
ΔP1	0.20
ΔF2	0.05
ΔP2	0.22

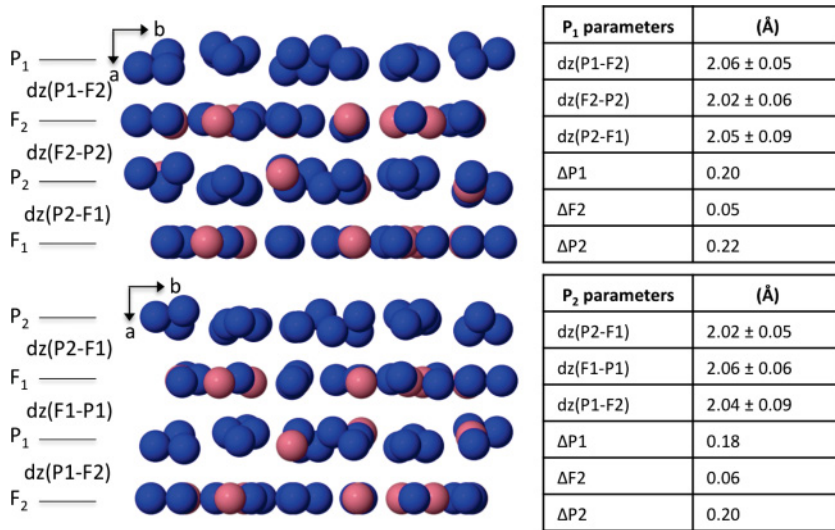| P₂ parameters	(Å)
dz(P2-F1)	2.02 ± 0.05
dz(F1-P1)	2.06 ± 0.06
dz(P1-F2)	2.04 ± 0.09
ΔP1	0.18
ΔF2	0.06
ΔP2	0.20

FIG. 9. (Color online) Relaxations of the surface layers of terminations P_1 and P_2 for the best-fit structure (4 in Table I). The dz parameters correspond to the average interlayer spacings, and the Δ parameters correspond to the puckering amplitude for each layer.

atoms, which is considerably better than the other terminations. Therefore, our conclusion from this LEED study is that the structure is a complete P-layer termination with no Co atoms, but with the presence of the glue atoms.

Figure 9 gives the relaxations of the surface layers in the best-fit terminations. There is a small amount of relaxation of the surface layers relative to the bulk structures. For the P_1 termination, the average relaxations are $+1\%$ and -1% for the first two layers, while the order is reversed for the P_2 termination, i.e. -1% and $+1\%$ for the first two layers. This reversal may seem unusual, but we recall that in the bulk structure, the two P layers are not identical because their puckering direction is reversed. This overall puckering is largely maintained in the surface structure, and the net effect at the surface appears to be that the intervening F layer resides closer to the P_2 layer than the P_1 layer in both terminations. Figure 9 shows the side-view drawings of the two terminations.

In Fig. 10, we present a histogram of all of the R-factor values, along with the spectra from the beams with the best and worst agreement. The individual R factors, the individual spectra and the final coordinates are all given in an supplementary material.[35]

V. DISCUSSION AND CONCLUSION

The STM results presented here indicate that the nature of the Al₁₃Co₄(100) surface may be dependent on the method of crystal growth. The main difference in the surfaces studied here appears to be the presence or absence of the glue atoms. On crystals of type 2, the fact that all glue atoms are present allows much higher resolution images to be obtained because the surface is flatter. On this surface, STM finds the best agreement with the DFT simulations of the P-termination model that has all Al atoms present, but with only the top Co atoms missing (structure model 3).

For the same sample type, LEED finds the best agreement for the P-termination model that has all Al atoms present, and no Co atoms in the top layer (structure model 4). There is a small amount (1%) of relaxation in the surface layers, which has the opposite sense for the two types of P terminations.

Otherwise, and aside from the missing Co atoms, the surface structure is quite similar to the structure of the corresponding bulk planes. For samples of type 2, both LEED and STM have effectively ruled out the F terminations and the P terminations in which the top Co atoms are present, or where nonglue Al atoms are missing. These experimental results are consistent with the DFT calculations, which find that structure models 3 and 4 are both stable surfaces.

The only disagreement, therefore, is in the preference for model 4 in the LEED result and the preference for model 3 in the STM result, and we would like to assess whether either technique can make a unique determination of the surface structure. The Pendry R factor from the LEED study for model 3 is 0.31, and for model 4, it is 0.26. Models yielding R factors greater than the optimum R factor $+$ RR [RR $=$ the variance of the Pendry R factor (Ref. 33)] can be significantly excluded based on statistical grounds. The RR factor is 0.01 for model 4, and therefore models having $R > 0.27$, including model 3, are very unlikely to be the true structure.

It is possible, however, that there is some actual difference in the samples studied by STM and LEED. While the samples used in the LEED and the STM type 2 studies gave similar LEED patterns, they were not the same crystal and were not grown in the same laboratory. The difference in the surface structures of the type 1 and type 2 samples grown using different methods and studied by STM is quite clear. Since the surface structure seems to be dependent on the details of the growth procedure, it is possible that the two samples used here in the STM and LEED studies are, in fact, different. The only resolution to this conundrum will be to carry out the two types of experiments on the same surface.

We also note that the LEED and STM techniques are quite different in their sampling of the surface structure. The STM measures local structures and can only sample small areas on the surface. It can be difficult to be sure that the areas measured are representative of the surface. LEED, on the other hand, measures over a relatively large area (up to 1 mm diameter) and therefore averages over all of the surface structures present. Since the diffraction intensities will be most intense for large well-ordered areas, the results may emphasize certain types
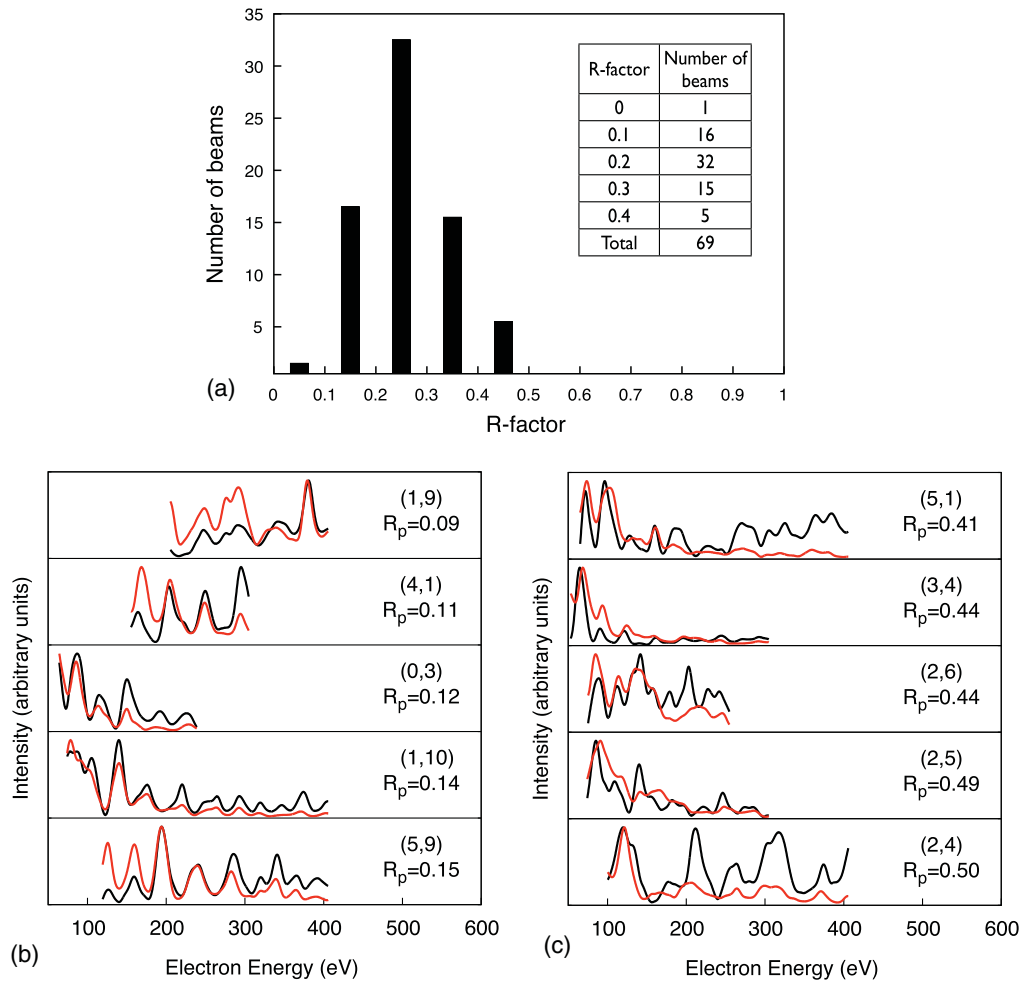
FIG. 10. (Color online) (a) Distributions of *R* factor for all beams in the best-fit structure. (b) best five beams, and (c) worst five beams of the experimental (black/bold) and best-fit calculated (red/light) LEED spectra, with individual *R* factors. The complete set of curves is given in the supplementary material (Ref. 35).

of areas over others. It is certainly possible that both of the surface terminations 3 and 4 are present on this surface.

We would like to emphasize the achievement of a reliable surface structure using LEED for this surface. As a comparison, the Al-Ni-Co fivefold surface has a quasiperiodic structure that is locally very similar to the $Al_{13}Co_4(100)$ surface. The amount of data that was obtained in LEED experiments on the quasicrystal surface is far less, requiring rather strict limitations on the structure models used in the analysis. Thus, although the *R* factors obtained in those studies ranged from 0.26 to 0.36,[36–38] the approximations required because of the smaller dataset effectively rule out a complete atomistic structure determination. In this paper, the large dataset in this study allows a complete atomistic structure determination. Nevertheless, there may be room for improvement in the LEED analysis. In this study, we have optimized each termination separately, comparing to the data obtained from a surface having both terminations. A better procedure would be to optimize the two terminations simultaneously with the experimental data. We are in the process of modifying the LEED programs to enable this method. Although we do not anticipate a large difference in

the final structure, a comparison of the methods will be very useful for future studies of such surfaces.

*Corresponding author: rdd2@psu.edu

[1] J. M. Dubois, *Useful Quasicrystals* (World Scientific Publishing Co., Singapore, 2003).

[2] M. Krajci and J. Hafner, Phys. Rev. B **71**, 184207 (2005).

[3] M. Krajci, J. Hafner, and M. Mihalkoviç, Phys. Rev. B **73**, 134203 (2006).

[4] T. Deniozou, R. Addou, A. K. Shukla, M. Heggen, M. Feuerbacher, M. Krajcí, J. Hafner, R. Widmer, O. Gröning, V. Fournée, J. M. Dubois, and J. Ledieu, Phys. Rev. B **81**, 125418 (2010).

[5] P. Gille and B. Bauer, Cryst. Res. Technol. **43**, 1161 (2008).

[6] M. Mihalkoviç and M. Widom, Phys. Rev. B **75**, 014207 (2007).

[7] W. Steurer, Mater. Res. Soc. Symp. **643**, K3.2.1 (2001).

[8] J. Grin, U. Burkhardt, M. Ellner, and K. Peters, J. Alloys Compd. **206**, 243 (1994).

[9] Y. Grin, B. Bauer, U. Burkhardt, R. Cardoso Gil, J. Dolinsek, M. Feuerbacher, P. Gille, F. Haarmann, M. Hegen, P. Jeglič, M. Müller, S. Paschen, W. Schnelle, and S. Vrtnik, presented at the *European Congress on Advanced Materials and Processes*, Nürnberg, Germany, 2007 (unpublished).

[10] M. Armbrüster, K. Kovnir, Y. Grin, and R. Schlögl, in *Complex Metallic Alloys: Basics and Applications* (Wiley-VCH, Berlin, 2010), p. 385.

[11] R. Addou, E. Gaudry, T. Deniozou, M. Heggen, M. Feuerbacher, P. Gille, Y. Grin, R. Widmer, O. Gröning, V. Fournée, J. M. Dubois, and J. Ledieu, Phys. Rev. B **80**, 014203 (2009).

[12] M. Gierer, M. A. Van Hove, A. I. Goldman, Z. Shen, S. L. Chang, C. J. Jenks, C. M. Zhang, and P. A. Thiel, Phys. Rev. Lett. **78**, 467 (1997).

[13] K. Pussi, M. Gierer, and R. D. Diehl, J. Phys. Condens. Matter **21**, 474213 (2009).

[14] H. I. Li, K. Pussi, K. J. Hanna, L. L. Wang, D. D. Johnson, H. P. Cheng, H. Shin, S. Curtarolo, W. Moritz, J. A. Smerdon, R. McGrath, and R. D. Diehl, Phys. Rev. Lett. **103**, 056101 (2009).

[15] G. Kresse and J. Furthmüller, Comput. Mater. Sci. **6**, 15 (1996).

[16] G. Kresse and J. Furthmüller, Phys. Rev. B **54**, 11169 (1996).

[17] G. Kresse and D. Joubert, Phys. Rev. B **59**, 1758 (1999).

[18] P. E. Blochl, Phys. Rev. B **50**, 17953 (1994).

[19] J. P. Perdew, K. Burke, and M. Ernzerhof, Phys. Rev. Lett. **77**, 3865 (1996).

[20] J. P. Perdew, K. Burke, and M. Ernzerhof, Phys. Rev. Lett. **78**, 1396 (1997).

[21] M. Widom and M. Mihalkoviç, Alloy Database at [http://alloy.phys.cmu.edu/], last update 23 July 2009, accessed on March 1, 2011.

[22] F. Fleischer, T. Weber, D. Y. Jung, and W. Steurer, J. Alloys Compd. **500**, 153 (2010).

[23] N. Moll, A. Kley, E. Pehlke, and M. Scheffler, Phys. Rev. B **54**, 8844 (1996).

[24] L. G. Dias, A. A. Leitao, C. A. Achete, R.-P. Blum, H. Niehus, and R. B. Capaz, Surf. Sci. **601**, 5540 (2007).

[25] F. Bechstedt, *Principles of surface physics* (Springer, Berlin, 2003).

[26] P. Jeglič, M. Heggen, M. Feuerbacher, B. Bauer, P. Gille, and F. Haarmann, J. Alloys Compd. **480**, 141 (2009).

[27] P. Jeglič, S. Vrtnik, M. Bobnar, M. Klanjšek, B. Bauer, P. Gille, Y. Grin, F. Haarmann, and J. Dolinšek, Phys. Rev. B **82**, 104201 (2010).

[28] W. R. Tyson and W. A. Miller, Surf. Sci. **62**, 267 (1977).

[29] F. R. De Boer, R. Boom, W. C. M. Mattens, A. R. Miedemia, and A. K. Neissen, *Cohesion in metals* (Elsevier, Amsterdam, 1988).

[30] X. Z. Xi, X. L. Li, and K. H. Kuo, Philos. Mag. Lett. **70**, 221 (1994).

[31] U. Burkhardt, M. Ellner, and Y. Grin, Z. Metallkd. **86**, 281 (1995).

[32] K. Saito, K. Sugiyama, and K. Hiraga, Mater. Sci. Eng. A **294-296**, 279 (2000).

[33] J. B. Pendry, J. Phys. C: Solid State **13**, 937 (1980).

[34] M. A. Van Hove, software download at [http://www.ap.cityu.edu.hk/personal-website/Van-Hove.htm#Download_software], last update 10 August 2011, accessed on March 1, 2011.

[35] See Supplemental Material at http://link.aps.org/supplemental/10.1103/PhysRevB.84.085411 for atomic coordinates plus a complete list of *R* factors, plotted spectra, and experimental and calculated intensities.

[36] K. Pussi and R. D. Diehl, Z. Kristallogr. **224**, 1 (2009).

[37] K. Pussi, N. Ferralis, M. Mihalkovic, M. Widom, S. Curtarolo, M. Gierer, C. J. Jenks, P. Canfield, I. R. Fisher, and R. D. Diehl, Phys. Rev. B **73**, 184203 (2006).

[38] N. Ferralis, K. Pussi, E. J. Cox, M. Gierer, J. Ledieu, I. R. Fisher, C. J. Jenks, M. Lindroos, R. McGrath, and R. D. Diehl, Phys. Rev. B **69**, 153404 (2004).